



# Large isotopic variability at the micron-scale in 'Shuram' excursion carbonates from South Australia

Jon M. Husson<sup>a,b,\*</sup>, Benjamin J. Linzmeier<sup>b</sup>, Kouki Kitajima<sup>b,c</sup>, Akizumi Ishida<sup>d,c</sup>, Adam C. Maloof<sup>e</sup>, Blair Schoene<sup>e</sup>, Shanan E. Peters<sup>b</sup>, John W. Valley<sup>b,c</sup>

<sup>a</sup> School of Earth and Ocean Sciences, University of Victoria, Victoria, BC V8W 2Y2, Canada

<sup>b</sup> Department of Geoscience, University of Wisconsin – Madison, WI, 53706, USA

<sup>c</sup> NASA Astrobiology Institute, Department of Geoscience, University of Wisconsin, Madison, WI, 53706, USA

<sup>d</sup> Department of Earth Science, Graduate School of Science, Tohoku University, Sendai 980-8578, Japan

<sup>e</sup> Department of Geosciences, Princeton University, Guyot Hall, Princeton, NJ 08544, USA

## ARTICLE INFO

### Article history:

Received 8 September 2019

Received in revised form 4 March 2020

Accepted 6 March 2020

Available online 17 March 2020

Editor: L. Derry

### Keywords:

carbon isotopes

SIMS

Shuram excursion

Ediacaran Earth history

## ABSTRACT

Ediacaran-aged (635–541 million years ago) marine sediments contain a large negative carbon isotope ( $\delta^{13}\text{C}$ ) excursion, in which carbonate  $\delta^{13}\text{C}$  values reach  $-12\text{‰}$  (VPDB). Known as the 'Shuram' excursion, many workers have interpreted this  $\delta^{13}\text{C}$  record as an unprecedented perturbation to the global carbon cycle, leading to speculation about a causal connection to the broadly contemporaneous rise of animal life. Others have interpreted the  $\delta^{13}\text{C}$  signal as a product of diagenesis, thereby minimizing its relevance for understanding the evolution of metazoans. Here, we present SEM imaging and in-situ  $\delta^{13}\text{C}$  and  $\delta^{18}\text{O}$  values measured by secondary ion mass spectrometry (SIMS) to assess these competing hypotheses in the Wonoka Formation of South Australia. Our results from the minimum of the excursion show that rounded sedimentary grains of calcite have  $\delta^{13}\text{C}$  values between  $-12.8$  to  $-10.6\text{‰}$  and  $\delta^{18}\text{O}$  values between  $-17.8$  to  $-15.5\text{‰}$  (VPDB). Euhedral dolomite that appears to have grown unimpeded in open sedimentary pore spaces also is present. These early-stage dolomites are interpreted as early authigenic in origin and have  $\delta^{13}\text{C}$  values that reach  $+5\text{‰}$ , requiring a formation fluid with a substantially different  $\delta^{13}\text{C}$  composition from basin waters or bulk sediment. Together, these results provide little evidence for the hypothesis that a late diagenetic overprint has generated the 'Shuram' excursion in the Wonoka. Instead, they suggest the presence of a large carbon isotopic gradient in the surface environment, with shallow waters capable of precipitating carbonates with very low  $\delta^{13}\text{C}$  (down to  $-12\text{‰}$ ) and deeper shelf and/or marine pore waters generating carbonates with positive carbon isotope values (up to  $+5\text{‰}$ ). Because negative isotope excursions of similar magnitude are found in widely dispersed Ediacaran basins, it is likely that this gradient was characteristic of shelf environments of this period and that a still-unknown global process led to the 'Shuram' excursion in shallow water carbonates.

© 2020 Elsevier B.V. All rights reserved.

## 1. Introduction

A fundamental goal for Earth system science is understanding the processes that led to the origin and diversification of animal life. The timing of metazoan origination remains a topic of debate, but their rise to abundance in the rock record is marked by the enigmatic 'Ediacaran Biota', which appeared  $\sim 570$  million years ago (Pu et al., 2016). Many hypotheses for the driver of animal evolution invoke a rise in atmospheric  $\text{O}_2$  across the Ediacaran–Cambrian transition (Lyons et al., 2014). Roughly contemporaneous

with these changes, extremely low carbon isotope values ( $\delta^{13}\text{C}$ ) are recorded in marine carbonates from Ediacaran basins around the world (Grotzinger et al., 2011). These isotopic profiles are coherent stratigraphically, reproducible, and can span hundreds of meters of vertical section, decreasing from  $\sim +3\text{‰}$  down to  $\sim -12\text{‰}$  before rising steadily back to  $\sim +4\text{‰}$  (all  $\delta^{13}\text{C}$  values are reported on the VPDB scale). Known colloquially as the 'Shuram' excursion, it is the most negative excursion of  $\delta^{13}\text{C}$  values known in Earth history. Whether the various 'Shuram' excursions are truly globally synchronous has yet to be tested independently via geochronology, although they are stratigraphically confined to the Ediacaran Period (Grotzinger et al., 2011).

No consensus model exists to explain the cause of the 'Shuram' excursion. Many interpret the excursion as a profound perturbation

\* Corresponding author at: School of Earth and Ocean Sciences, University of Victoria, Victoria, BC V8W 2Y2, Canada.

E-mail address: jhusson@uvic.ca (J.M. Husson).

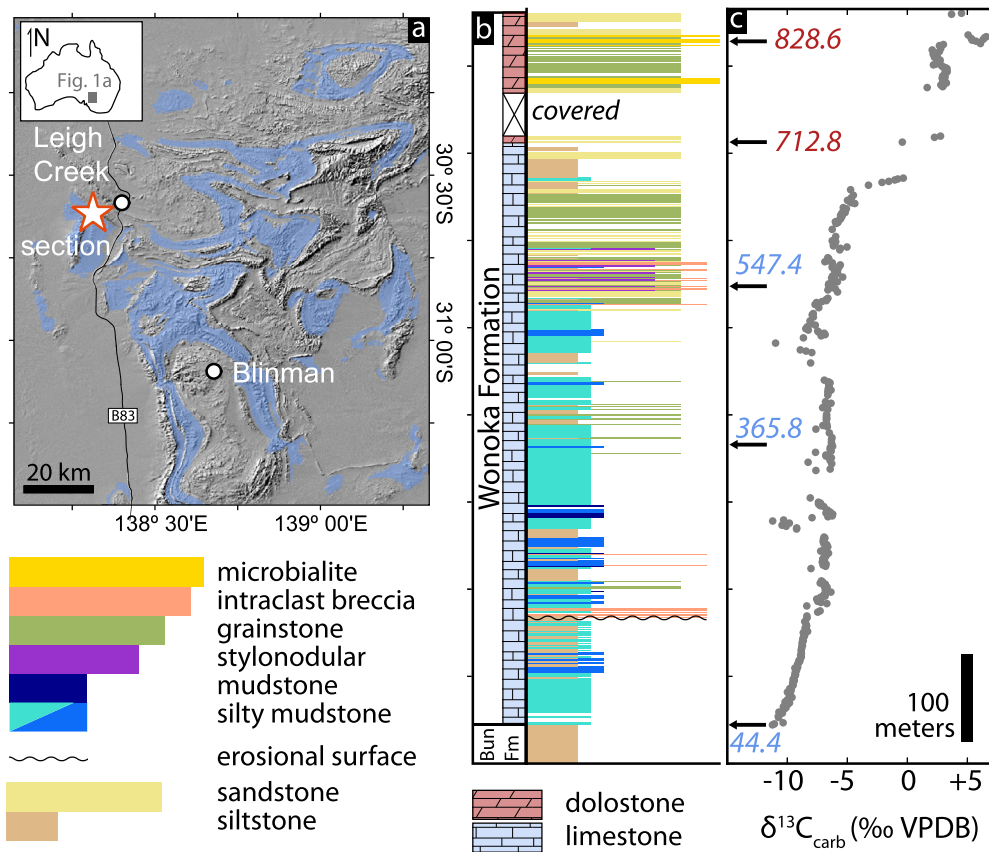


**Fig. 1.** (a) Geologic map of the Wilpena Group, which includes the Wonoka Formation. The map was created via the Macrostrat API (Peters et al., 2018) using data from Geoscience Australia (Raymond et al., 2012) and the Shuttle Radar Topography Mission (Farr et al., 2007). The study locality (measured section 9 from Husson et al., 2015b) is marked with a star. Base of section located at 30° 36.964'S, 138° 18.762'E (WGS84). The physical stratigraphy (b) and carbon isotope (c) chemostratigraphy of the uppermost Bunyeroo (abbreviated 'Bun. Fm.') and Wonoka formations are modified from Husson et al. (2015b). On panel (c), small arrows and colored numbers indicate the horizons analyzed by SIMS (blue numbers are limestones, red are dolostones). (For interpretation of the colors in the figure(s), the reader is referred to the web version of this article.)

to the global carbon cycle and an epiphenomenon that accompanied the transition to a more oxic Earth surface (Rothman et al., 2003; Fike et al., 2006). In such a scenario, rising levels of surface oxidants led to the remineralization of a reservoir (or reservoirs) of organic carbon, which subsequently drove global dissolved inorganic carbon (DIC) isotopically negative (Rothman et al., 2003). Models, however, note the unreasonably high oxidant demands required to drive the 'Shuram' excursion as a global perturbation if it lasted for millions of years, along with its deleterious effects on climate (Bristow and Kennedy, 2008). These considerations, along with a puzzling correlation between  $\delta^{13}\text{C}$  and  $\delta^{18}\text{O}$  values in 'Shuram' excursion carbonates (Grotzinger et al., 2011), have formed the basis for models that contend that the extremely negative  $\delta^{13}\text{C}$  values are diagenetic in origin (Knauth and Kennedy, 2009; Derry, 2010; Schrag et al., 2013), and thus disconnected from global DIC.

Determining the cause of the 'Shuram' excursion has important implications both for understanding Earth history and the origins of animals, as well as for the general utility of carbon isotope profiles as inter-basin correlation tools (e.g., Halverson et al., 2005). Styles of diagenesis invoked to explain the 'Shuram' include meteoric alteration (Knauth and Kennedy, 2009), burial diagenesis (Derry, 2010) and the growth of isotopically-depleted authigenic carbonate ( $\text{CaCO}_3$  that grows in-situ at or near the sediment-water interface, Schrag et al., 2013). Each is a mixing model, wherein varying admixtures between primary and secondary carbonate give rise to the bulk stratigraphic signal. Testing these ideas has most often relied upon developing isotopic datasets and interpreting them in the context of field relationships and sedimentological arguments (e.g., Le Guerroué et al., 2006; Husson et al., 2015b).

For example, in South Australia, the Ediacaran-aged Wonoka Formation (Fig. 1a) contains a basin-wide 17‰ excursion in  $\delta^{13}\text{C}$  values, with values starting at -12‰ at its base and changing smoothly to +5‰ at its top (Fig. 1b and c, Husson et al., 2015b). In the more distal parts of the basin, the formation hosts penecon-temperaneous paleocanyons that incise up to 1 km down into the underlying stratigraphy (Von der Borch et al., 1982), filled in part with tabular-clast carbonate breccias. Within single meter-scale deposits, these redeposited clasts show the same  $\delta^{13}\text{C}$  values as the intact canyon-shoulder sections, requiring that the negative  $\delta^{13}\text{C}$  values (and the correlation with  $\delta^{18}\text{O}$ ) were acquired in these Ediacaran carbonates *before* brecciation and redeposition as canyon-fill (Husson et al., 2012). These *isotope conglomerate tests* rule out late-stage alteration for the negative carbon isotope values observed from the Wonoka Formation, but diagenetic processes that occur before significant burial remain allowable (Grotzinger et al., 2011).

The vast majority of published  $\delta^{13}\text{C}$  values measured from carbonates have used conventional acid digestion and gas-source mass spectrometry (GSMS), which produce 'bulk' isotopic profiles. This approach has demonstrated that the 'Shuram' excursion signal is reproducible across certain basins (e.g., Husson et al., 2015b; Le Guerroué et al., 2006), and spatially variable in others (Macdonald et al., 2013; Li et al., 2017; Cui et al., 2017). Regardless, bulk sampling methodology makes it impossible to determine grain-scale geochemical differences and prevents the identification of isotopically distinct phases of carbonate – for example, sedimentary grains with a typical marine  $\delta^{13}\text{C}$  value ( $\sim 0\text{‰}$ ) mixed with diagenetic phases (e.g., void-filling cements, dolomite) with nega-

tive  $\delta^{13}\text{C}$  values ( $\sim -20\text{‰}$ ). Depending upon their volumetric importance, diagenesis may have affected the bulk rock  $\delta^{13}\text{C}$  value while leaving behind a detectable primary signal at the grain-scale.

Secondary ion mass spectrometry (SIMS) allows the  $\delta^{13}\text{C}$  and  $\delta^{18}\text{O}$  values of multiple carbonate phases within the same sample to be measured. When combined with scanning electron microscopy (SEM), SIMS can quantify the isotopic composition of individual grains and crystals of carbonate phases that are identified by their petrography (Śliwiński et al., 2016a,b, 2017). Measurements of  $\delta^{13}\text{C}$  values by SIMS have been made on ooids and two generations of calcite cements in Shuram Formation carbonates from Oman (Bergmann, 2013). These three populations overlap isotopically at the  $1\sigma$  level (population means of each are  $\approx -9\text{‰}$ ), and these agreements were interpreted as evidence of a rock-buffered system during cementation and a primary origin for the bulk isotope signature (Bergmann, 2013). The Zhongling section of the Ediacaran-aged Doushantuo Formation in South China also has SIMS measurements (Cui et al., 2019), an unusual locality with both a dolomitic phase ( $\delta^{13}\text{C}$  values of  $-1\text{‰}$  to  $+6\text{‰}$ ) and cm-scale, calcite nodules ( $\delta^{13}\text{C} = -37\text{‰}$  to  $-5\text{‰}$ , Cui et al., 2017). The SIMS and SEM results have been used as evidence that these calcite nodules are authigenic, formed early, and contributed to generating the 'Shuram' excursion (Cui et al., 2019). Here, we test these competing hypotheses by extending the SIMS work from these basins to the Wonoka Formation of South Australia (Fig. 1a), one of the first successions identified as containing the 'Shuram' excursion (Calver, 2000).

## 2. Methods

### 2.1. Sample selection

The Wonoka Formation is  $\sim 500$  to  $\sim 800$  m thick, and consists of a shallowing-upward sequence of mixed carbonates and siliciclastics (Fig. 1b, Husson et al., 2015b). The succession predominantly consists of limestones, except for the uppermost 5–100 m, where dolostones are present. Five samples from one measured section (Fig. 1b) were selected for analysis by SIMS. The samples span the range of observed bulk  $\delta^{13}\text{C}$  values and depositional facies (arrows on Fig. 1c), with the sample numbers corresponding to stratigraphic height in meters above datum. The lowermost sample (44.4) is from an interval of thin-bedded (2–5 cm) calciturbidites. The following two (365.8 and 547.4) are from the more carbonate-rich and coarser-grained portion of the stratigraphy, consisting of swaley cross-stratified grainstones. All three are limestones. Sample 712.8 is a dolomite-cemented sandstone, and 828.6 is a micro-bialitic dolostone.

### 2.2. In-situ carbonate $\delta^{13}\text{C}$ and $\delta^{18}\text{O}$ microanalysis by SIMS

Carbon ( $\delta^{13}\text{C}$ ) and oxygen ( $\delta^{18}\text{O}$ ) isotope values of micrometer-scale domains were measured in-situ using a CAMECA IMS 1280 large-radius multi-collector ion microprobe at the WiscSIMS Laboratory (Department of Geoscience, University of Wisconsin-Madison). Samples cast into 25 mm diameter epoxy rounds (Fig. S1) were flattened using diamond embedded pads and polished using polycrystalline diamond and alumina suspensions. Low surface relief ( $< \sim 2\text{ }\mu\text{m}$ ) is a requirement, as sample topography is a source of mass fractionation during ion sputtering that degrades both accuracy and precision (Kita et al., 2009). Samples were first examined by high-resolution back-scattered electron (BSE) SEM-imaging, energy-dispersive X-ray spectroscopy (EDS) and cathodoluminescence (CL) imaging under an iridium coat to identify different phases of carbonate present in each sample. Mounts then were cleaned by ultrasonication in alternating baths

(3 cycles) of ethanol and deionized water, dried overnight in a vacuum oven at  $40^\circ\text{C}$  and sputter-coated with a layer of gold ( $\sim 20$  nm thick) to assist charge compensation during SIMS analysis.

Carbon measurements were performed with a primary  $^{133}\text{Cs}^+$  beam with an intensity of 0.4 nA and total impact energy of 20 keV, focused on 6  $\mu\text{m}$ -diameter spot-sizes on the sample surface. Spot-sizes of 10  $\mu\text{m}$ -diameter were used for oxygen, using a 1.0 nA  $^{133}\text{Cs}^+$  beam with total impact energy of 20 keV. Boring depths for each are 1–2  $\mu\text{m}$ . An electron gun was used to provide charge compensation. Instrument configurations have been described in detail previously (Valley and Kita, 2009; Śliwiński et al., 2016a,b, 2018). For  $\delta^{13}\text{C}$  and  $\delta^{18}\text{O}$ , precision on an individual value is  $0.4\text{--}1.0\text{‰}$  ( $2\sigma$ ) and  $0.2\text{--}0.4\text{‰}$  ( $2\sigma$ ), respectively. Here, precision is defined by replicate measurements ( $n = 8$ ) of drift monitors UWC-3 (calcite, Kozdon et al., 2009) and UW6220 (dolomite, Śliwiński et al., 2016a,b) which bracketed each set of approximately 10 sample analyses (analytical accuracy is addressed separately further below).

After SIMS, the major cation chemistry of the analyzed domains (Ca, Mg, Fe, Mn and Sr abundances) was characterized by electron probe microanalysis (EPMA) by a CAMECA SX-51 (Cameron Electron Microprobe Laboratory, Department of Geoscience, University of Wisconsin-Madison). This step is required to correct for instrument bias caused by the chemical composition of an analyzed phase. Several different suites of carbonate reference materials (RMs) were measured at the beginning of the analytical session (Fig. S2), so that the magnitude of the  $\delta^{13}\text{C}$  and  $\delta^{18}\text{O}$  biases (i.e., the matrix-effects) could be calibrated to cation composition. The RMs measured include the dolomite-ankerite series (Śliwiński et al., 2016a,b) and two calcite standards with differing minor-element (Mg, Fe, Mn, Sr) composition: UWC-3 (Kozdon et al., 2009) and UWC-4 (Turnier et al., 2020), a Fe- and Mn-bearing calcite (Tables S1–S4).

The cation compositions of the analyzed unknowns and reference materials are shown in Figs. 2 and S3. For both  $\delta^{13}\text{C}$  and  $\delta^{18}\text{O}$ , the composition and measured mass bias of each RM was plotted in 3-D space ( $\text{XCa}$ ,  $\text{X(Fe+Mn)}$ , SIMS mass bias) and a surface model (thin-plate spline fit) was applied so that a bias correction factor for each sample measurement could be interpolated based on its EPMA-measured chemistry. The bias calibration models are shown as contoured ternary plots in Fig. 2. Variability ( $2\sigma$ ) in the  $\delta^{13}\text{C}$  bias correction factors applied to sample unknowns is  $\pm 0.5\text{‰}$  for calcites and  $\pm 0.9\text{‰}$  for dolomites. For  $\delta^{18}\text{O}$  corrections, variability is  $\pm 0.5\text{‰}$  (calcite) and  $\pm 2.6\text{‰}$  (dolomite), with the larger spread in the latter due primarily to variability in Fe-Mn content (Fig. 2b). A comparison of measured RM  $\delta^{13}\text{C}$  and  $\delta^{18}\text{O}$  values against those predicted by the surface model (Tables S5 and S6) indicates SIMS measurement accuracy of  $0.5\text{‰}$  for both  $\delta^{13}\text{C}$  and  $\delta^{18}\text{O}$  values, in relation to the certified reference material NIST-19. Further details about these data reduction methodologies can be found in Valley and Kita (2009) and Śliwiński et al. (2016a,b, 2018).

The SIMS dataset includes 151  $\delta^{13}\text{C}$  values (from all five samples, Fig. 1c) and 71  $\delta^{18}\text{O}$  values (from samples 44.4 and 828.6). These totals include 42 paired analyses - i.e., carbonate grains/crystals on which both measurements were made. Producing paired data for the full dataset is not possible, because some domains are too small to accommodate two spots (lengthscale  $\leq 15\text{ }\mu\text{m}$ ). Imagery from BSE was integrated with SIMS and EPMA data using QGIS (Linzmeier et al., 2018). Images of all SIMS pits are provided in Figs. S4–S16, and all data (including uncorrected and corrected SIMS values) are provided in a supplementary Excel file. The sample mounts are stored at the University of Wisconsin Geology Museum with these identifiers: 44.4 = UWGMG 4989, 365.8 = UWGMG 4990, 547.4 = UWGMG 4991, 712.8 = UWGMG 4992, 828.6 = UWGMG 4993.

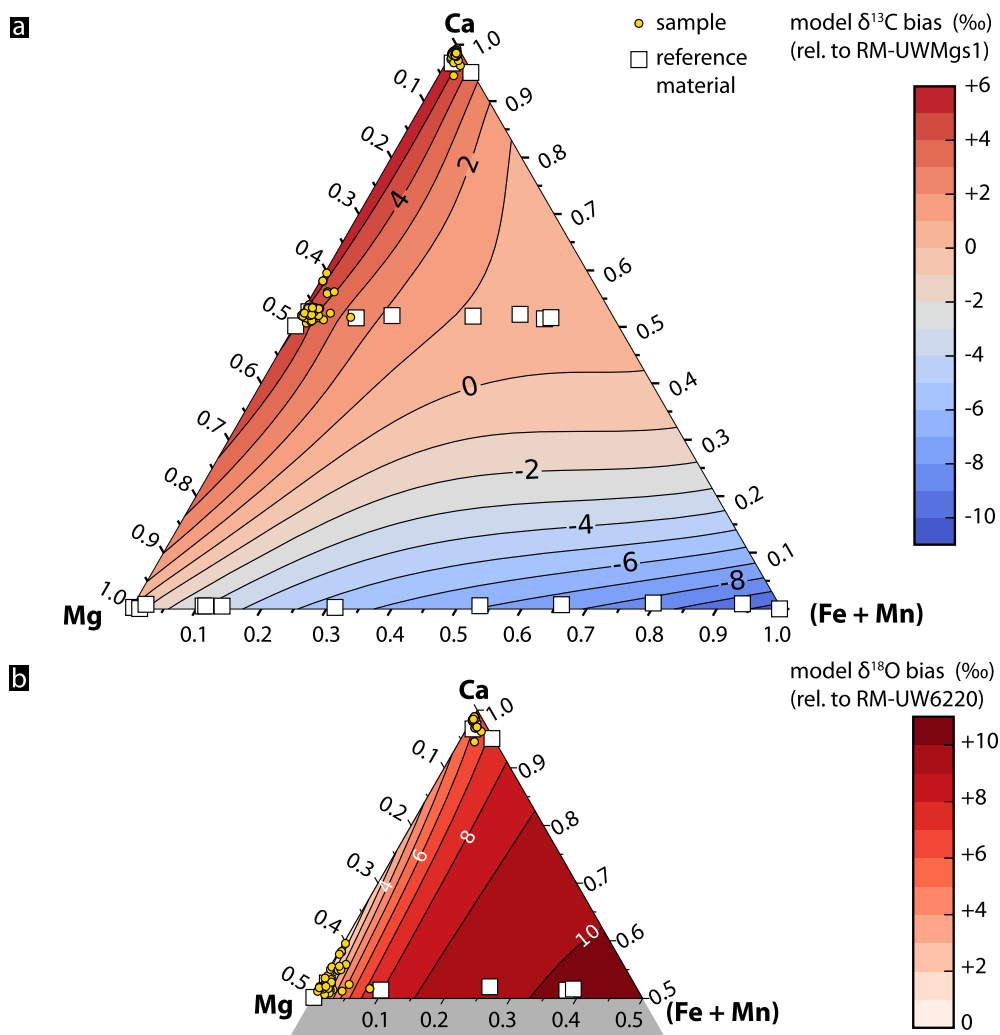


**Fig. 2.** Carbonate ternary diagram [Ca-Mg-(Fe+Mn)] showing modeled SIMS  $\delta^{13}\text{C}$  (a) and  $\delta^{18}\text{O}$  (b) bias contours (Śliwiński et al., 2018). RMs are plotted as white squares, and samples as yellow dots. The  $\delta^{13}\text{C}$  bias magnitude is expressed relative to that of end-member magnesite (UWMgs1, Table S5), and the  $\delta^{18}\text{O}$  magnitude is expressed relative to dolomite standard UW6220 (Table S6).

### 3. Results

#### 3.1. Petrography and elemental geochemistry

Understanding the Wonoka SIMS results requires considering them in a petrographic context. Sample 44.4 includes an erosive contact (dashed red line in Fig. 3a) between a more carbonate-rich layer (lower, brighter region) and more siliciclastic-rich layer (upper, darker region). These regions also are apparent on BSE imagery, in which brightness correlates with the average atomic number of an imaged phase. Thus generally, silicates are dark and carbonate minerals are brighter (Fig. 3b). The carbonate portion can be further delineated into four distinct phases (Fig. 3c, d and e). The most abundant phases by volume are two types of calcite (darker and lighter gray on Fig. 3e), where the brightness contrast is controlled by Mn content. Most dark calcite spots ( $n = 13$ ) have no measurable amount of Mn (EPMA detection limit  $\approx 200$  ppm), and the remainder have Mn levels between 740 and 5,600 ppm ( $n = 7$ ). The three highest Mn measurements (6,500 to 12,500 ppm) are from spots on the bright calcite phases identified under BSE (Fig. 3e and supplementary Excel file).

Dolomites also are present, but are rarer than calcite and unevenly distributed throughout the sample. Within the siliciclastic-rich layer, dolomites constitute 19% of the total carbonate fraction, as measured by 351 points counted from a 3 mm<sup>2</sup> portion of the

sample mount. Within the carbonate-rich layer, dolomites represent only 3% of total carbonate. Each dolomite observed under BSE has a darker core mantled by a brighter rim (Fig. 4). These differences are controlled by cation chemistry, namely: (a) the rims are more Ca-rich compared to the cores (mean Ca/Mg molar ratio of 1.32 vs. 1.12) and (b) the concentration of Fe+Mn, with rims containing an average of 2.20% end-member  $(\text{Fe+Mn})\text{CO}_3$  and cores with an average of 0.54% (molar percentages). Thus, dolomite rims have higher average atomic weights than cores. While many cores have planar edges with angular corners (Fig. 4b–f), others have more irregular, anhedral boundaries (Fig. 4g–k). Some grains are combinations: planar where the darker dolomite defines a grain edge, and irregular where mantled by the lighter dolomite (Fig. 4a). Based on 238 observed dolomites, 45% have anhedral cores.

Dolomite is absent from the next two limestone samples, 365.8 and 547.4, which consist entirely of calcite and siliciclastics (Fig. 5a and b). Sample 547.4 has less siliciclastic material than either 365.8 or 44.4, consistent with the overall stratigraphic trend of increasing carbonate content upwards (Fig. 1b). The carbonate component in each consists of interlocking grains of angular calcite. Both samples also lack clear compositional differences within the calcite fraction – unlike sample 44.4, which showed darker, Mn-poor calcite and brighter, Mn-rich calcite under BSE (Fig. 3e). Petrographic het-



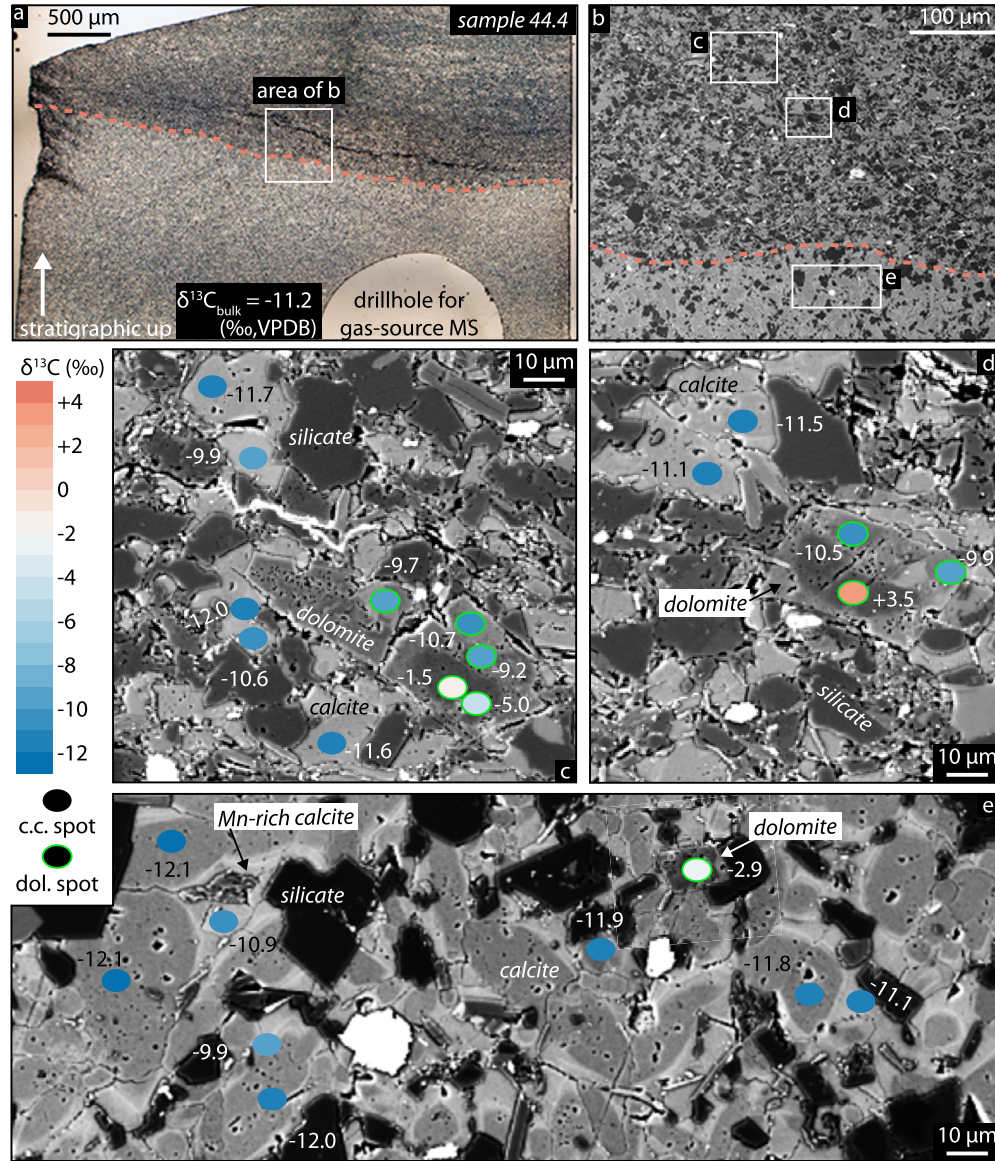


**Fig. 3.** Reflected light (a) and BSE images (b) showing an overview of sample 44.4. (c–e) BSE images with the size, shape and location of each oval corresponding to a 6  $\mu\text{m}$  wide  $\delta^{13}\text{C}$  SIMS pit. Each is color-coded and labeled according to its  $\delta^{13}\text{C}$  value. Dots with green outlines are on dolomite (“dol. spots” in the legend), whereas dots with no outlines are calcite (“c.c. spots”).

erogeneity returns with the first appearance of pervasive dolomitization in the Wonoka with sample 712.8, a dolomite-cemented sandstone (Fig. 1b). Under BSE, darker rims of dolomite are shown mantling generally lighter, structureless dolomite (Fig. 5c). Similar to the dolomites in sample 44.4, these BSE brightness differences are controlled by Fe+Mn content, with the darker rims containing an average of 0.87% (Fe+Mn) $\text{CO}_3$ , compared to 1.35% in the brighter dolomite. The uppermost sample analyzed (828.6) is a microbialitic dolostone that also contains two generations of dolomite identifiable under BSE: a more coarsely crystalline phase with clear zonation (upper left of Fig. 5d) and a finer-grained dolomite that is darker generally (bottom half of Fig. 5d).

### 3.2. SIMS carbon isotope geochemistry

Each type of carbonate described above was measured by SIMS. Unless otherwise stated, all isotopic values discussed below were obtained by SIMS. On Fig. 3c–e and on Fig. 5, each oval is the size, shape and location of a SIMS analysis, color-coded by its  $\delta^{13}\text{C}$  value. Both the GSMS and the SIMS values are shown together

on Fig. 6a, with the latter displayed as kernel density estimates (KDEs). Summarized in this way, there are two types of results. One set has unimodal, tight distributions of  $\delta^{13}\text{C}$  values (365.8, 547.4 and 828.6;  $2\sigma$  of each distribution is 1.0, 1.4, and 1.2‰, respectively). Each distribution is centered on or within  $\sim 1\%$  of the GSMS  $\delta^{13}\text{C}$  value. The other samples (44.4 and 712.8) are much more complex. Sample 712.8 roughly is bimodal, with one mode centered on  $-1.3\%$  and the other on  $+3.8\%$  (range is  $-2.3$  to  $+5.3\%$ ). Sample 44.4 has the highest variance, with a dominant mode that straddles the GSMS  $\delta^{13}\text{C}$  value of  $-11.2\%$  and a long tail of more positive values that reaches  $+7\%$ .

When  $\delta^{13}\text{C}$  values are parsed by mineralogy, clear patterns emerge. In Fig. 6b–f,  $\delta^{13}\text{C}$  values are binned by the different carbonate phases described above. In sample 44.4 (Fig. 6f), both Mn-poor ( $<1000$  ppm Mn, as measured by EPMA) and Mn-rich calcite have values close to the GSMS  $\delta^{13}\text{C}$  value of  $-11.2\%$  (population mean  $\pm 2\sigma$ :  $-11.8 \pm 1.1\%$  and  $-10.7 \pm 1.1\%$ , respectively). The dolomite rims have a higher mean  $\delta^{13}\text{C}$  value than the calcite populations ( $-10.0 \pm 1.1\%$ ). Dolomite cores have the highest  $\delta^{13}\text{C}$

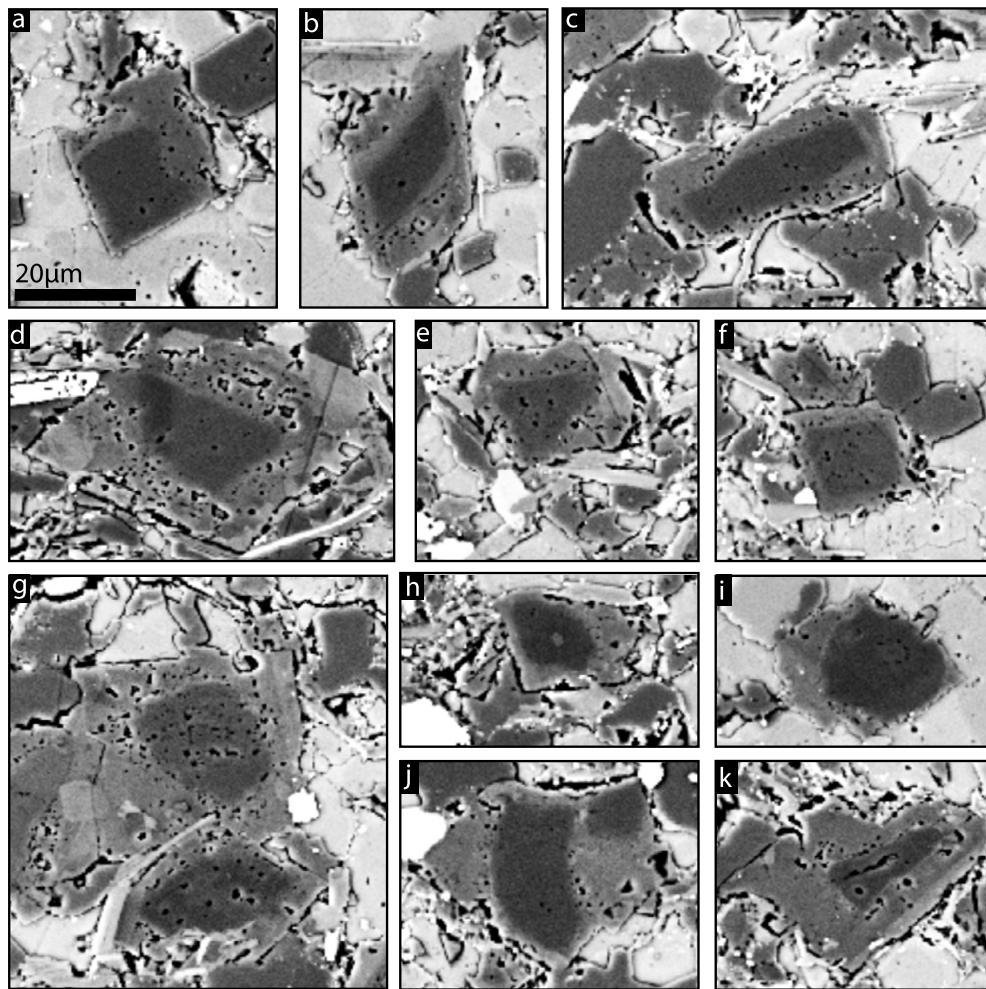


**Fig. 4.** BSE images of dolomites from sample 44.4, each exhibiting a dark core and lighter rim (controlled by higher Ca, Fe and Mn content in the rims). Some cores have angular edges (a–f) while others are more irregular (g–k).

values, which range from  $-5.0$  to  $+4.9\text{‰}$ . The one exception is a single calcite measurement (analysis 993), which is the most positive  $\delta^{13}\text{C}$  value ( $+6.7\text{‰}$ ) measured in sample 44.4. It is far outside the distributions of the other calcite spots ( $-11.4 \pm 1.4\text{‰}$ , Fig. 6f).

To investigate whether this measurement is real or an analytical artifact, we analyzed 3 spots surrounding this anomalous value on the same calcite grain (Fig. S4). The isotopic values of the three companion spots are  $-11.3\text{‰}$ ,  $-11.3\text{‰}$  and  $-11.0\text{‰}$ , and thus overlap within analytical uncertainty ( $\sim 0.7\text{‰}$ ) and with the overall calcite  $\delta^{13}\text{C}$  distribution from this sample (Fig. 6f). These observations suggest that analysis 993 is an anomalous outlier of currently unknown origin. While SEM images do not show any irregularities in pit morphology (Fig. S4), it remains possible that this analysis hit a crack or cavity below the sample surface, leading to anomalous beam behavior caused by surface roughness (Kita et al., 2009). Given that all other  $\delta^{13}\text{C}$  values in sample 44.4 are well organized by mineralogy (i.e., calcite vs. dolomite) and major cation chemistry (i.e., dolomite rims vs. dolomite cores), we find an  $18\text{‰}$  isotopic gradient within a single grain of otherwise homogeneous calcite (Fig. S4) to be unlikely.

The next two up-section samples (365.8 and 547.4, both limestones) have populations of  $\delta^{13}\text{C}$  values with much lower variance in (Fig. 6a, d, e). The distribution from sample 365.8 ( $-5.4 \pm 1.0\text{‰}$ ) is unimodal, but offset by  $\sim 1\text{‰}$  from its bulk value ( $-6.3\text{‰}$ ). Analyses from sample 547.4 also form a single population ( $-6.0 \pm 1.4\text{‰}$ ), but its mean is closer to the bulk value ( $-6.3\text{‰}$ ). Such tight distributions are consistent with compositional homogeneity

as indicated by BSE (Fig. 5a, b). High variance returns with the first appearance of pervasive dolomitization in the Wonoka with sample 712.8 (Fig. 1b), a dolomite-cemented sandstone. Values range from  $-2.3$  to  $+5.3\text{‰}$ , with the darker, dolomite rims being more tightly clustered ( $-1.6$  to  $+0.9\text{‰}$ ) and occupying the more negative end of the full distribution (Fig. 6c). Within each type of dolomite, the observed variability (range of  $7\text{‰}$  in the lighter dolomite,  $2.5\text{‰}$  in the rims) does not correlate with any coherent compositional patterns seen under BSE (Fig. 5c). This finding contrasts with samples 365.8 and 547.4, which show both compositional homogeneity and low variance in distributions of  $\delta^{13}\text{C}$  values. The uppermost sample analyzed (828.6) has a unimodal  $\delta^{13}\text{C}$  distribution ( $+6.3 \pm 1.2\text{‰}$ ), centered close to its GSMS value of  $+5.7\text{‰}$ , with no difference in  $\delta^{13}\text{C}$  values between the zoned ( $+6.3 \pm 1.0\text{‰}$ ) and finer-grained dolomite ( $+6.2 \pm 1.3\text{‰}$ ).

### 3.3. SIMS oxygen isotope geochemistry

Values of  $\delta^{18}\text{O}$  (reported here on the VPDB scale) were acquired by SIMS on the four types of carbonate present in sample 44.4 (calcite, Mn-rich calcite, dolomite rims and dolomite cores, Fig. 7a) and the two present in sample 828.6 (fine-grained and zoned dolomite, Fig. 7b). In sample 44.4,  $\delta^{18}\text{O}$  values of calcite and Mn-calcite are similar to one another. Population means ( $\pm 2\sigma$ ) are  $-17.1 \pm 1.5\text{‰}$  and  $-16.4 \pm 1.6\text{‰}$ , respectively, with the latter excluding one outlier which may be a mixed analysis between calcite and silicate (Fig. S7). These populations means are more negative



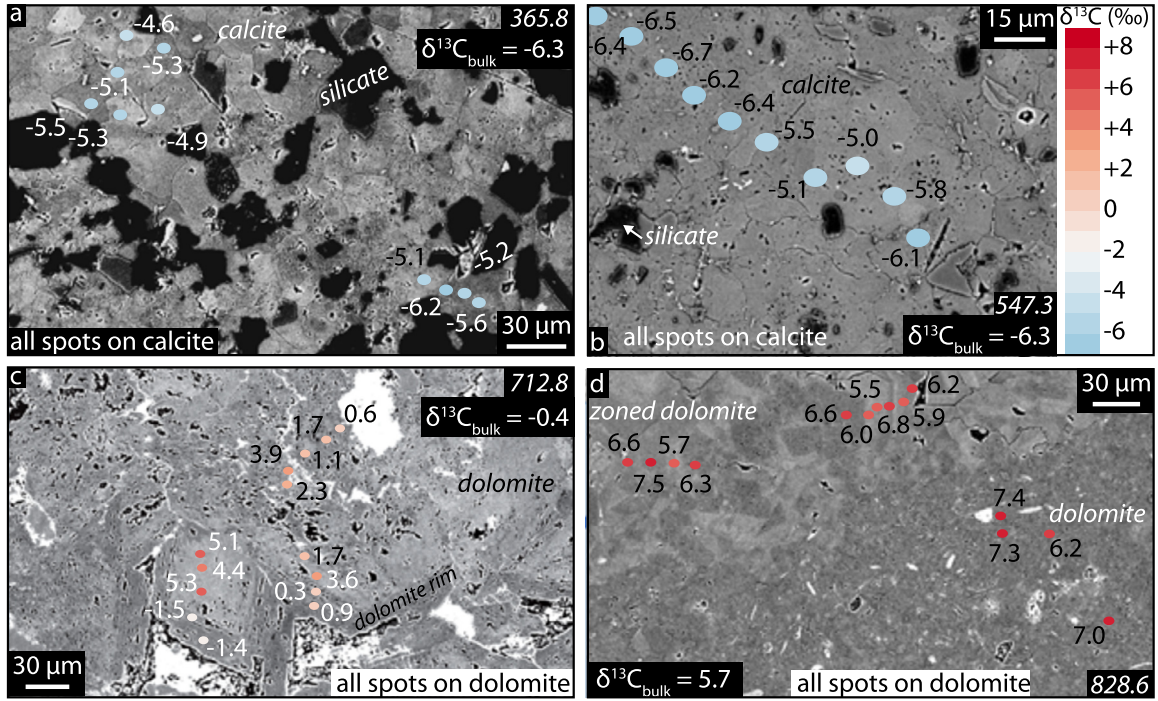


**Fig. 5.** BSE images of samples 365.8 (a), 547.3 (b), 712.8 (c) and 828.6 (d) showing regions with SIMS measurements of  $\delta^{13}\text{C}$  values, with the size, shape and location of each oval corresponding to a 6  $\mu\text{m}$  wide SIMS pit. Each is color-coded and labeled according to its  $\delta^{13}\text{C}$  value.

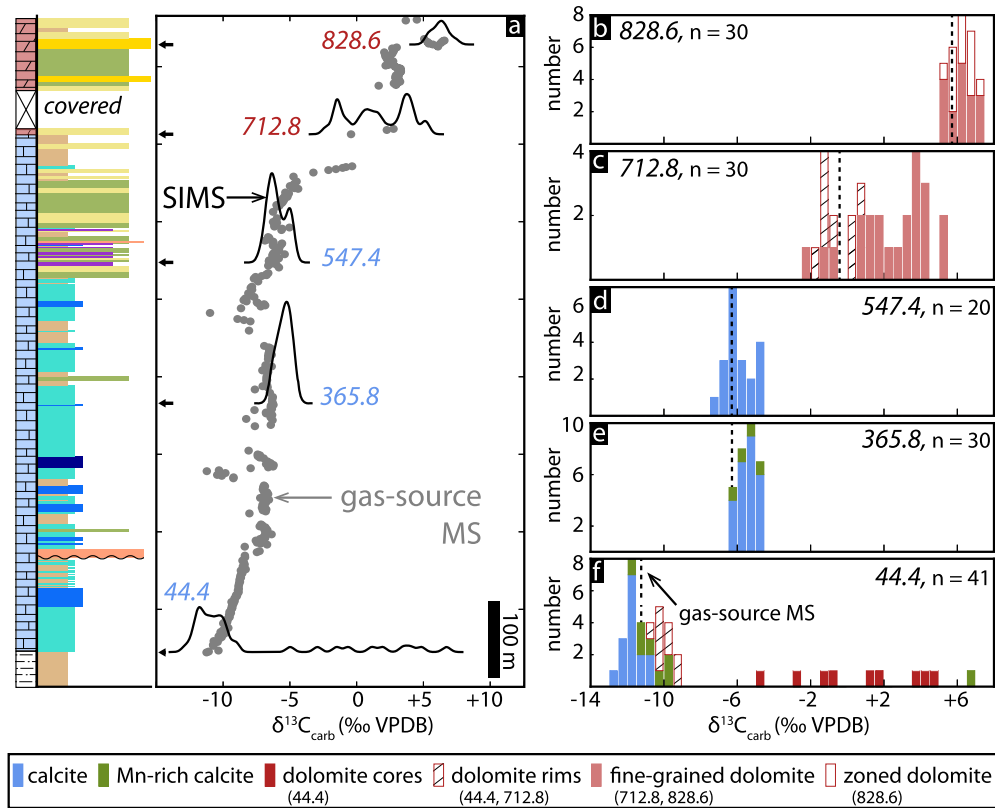


**Fig. 6.** (a) Summary results of both bulk-GSMS and SIMS microanalyses of  $\delta^{13}\text{C}$  values in the Wonoka Formation. Gray dots are GSMS measurements (Husson et al., 2015b) and black curves are kernel density estimates (KDEs) of the SIMS results from the five labeled horizons (blue numbers are limestones, red are dolostones), and stratigraphic lithofacies log is simplified from Fig. 1b. While the base of each KDE aligns with its corresponding stratigraphic position, the heights of the peaks are arbitrary with respect to the y-axis. Small arrows to the left of each KDE also points to each sample's stratigraphic height. (b–f) Histograms of the SIMS results, organized by stratigraphic height. Different box colors and fill patterns correspond to different phases/types of carbonate from a given sample. Here, Mn-rich calcite is defined as having  $[\text{Mn}] > 1000$  ppm as measured by EPMA, as opposed to BSE image interpretation (see also Fig. S18 for a cross-plot between  $[\text{Mn}]$  and  $\delta^{13}\text{C}$  in sample 44.4).

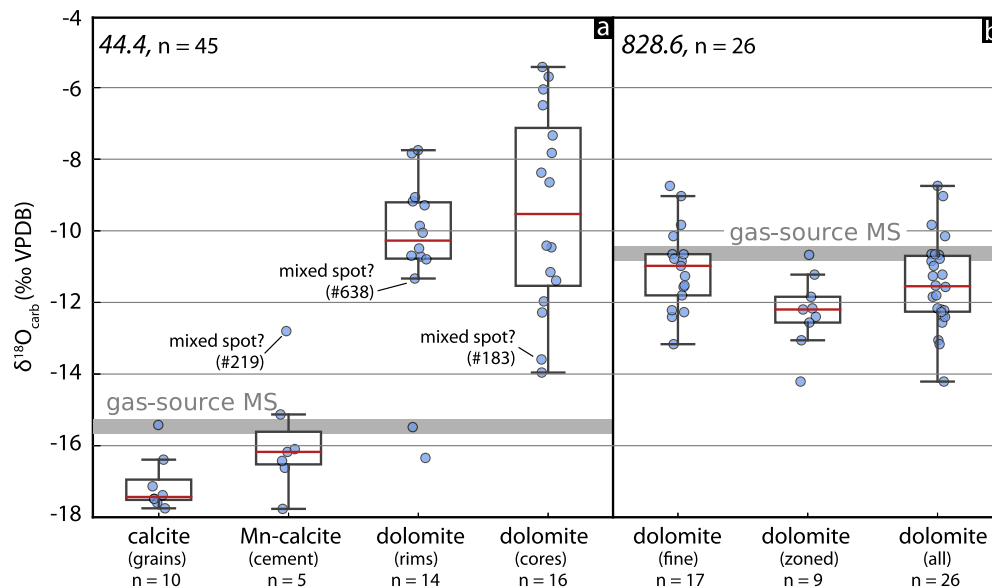


**Fig. 7.** Box-whisker plots of SIMS microanalyses of  $\delta^{18}\text{O}$  values in samples 44.4 and 828.6, organized by different phases/types of carbonates as in Fig. 6b–f. Based on BSE images, the three labeled data are from spots that may be mixtures between dolomite core and dolomite rim (analysis number 183, Fig. S7) and carbonate and silicate (analyses 219 and 638, Fig. S5 and S8). Note that the GSMS data are from powders that homogenized all carbonates and thus reflect the mineral mode, while SIMS data are compositions of specific generations of carbonate and are not intended to represent the average for the rock. Thus the SIMS data are verified by conventional GSMS analyses and show the true variability within a sample.

than the GSMS  $\delta^{18}\text{O}$  value for sample 44.4 ( $-15.5\text{‰}$ ). Values from dolomite rims and cores are much more dispersed ( $-10.6 \pm 4.8\text{‰}$  and  $-9.4 \pm 5.5\text{‰}$ , respectively), with population means more positive than the GSMS value (Fig. 7a). In sample 828.6, the population of  $\delta^{18}\text{O}$  values from fine-grained dolomite ( $-11.1 \pm 2.3\text{‰}$ ) is centered near the GSMS value ( $-10.6\text{‰}$ ), whereas zoned dolomites have a population mean more negative than the bulk composition ( $-12.3 \pm 2.0\text{‰}$ ).

## 4. Discussion

### 4.1. Values of $\delta^{13}\text{C}$ and petrographic patterns in carbonates of the Wonoka Formation

Given the precision of an individual  $\delta^{13}\text{C}$  analysis ( $0.4\text{--}1.0\text{‰}$ ) and the accuracy of SIMS results (within  $0.5\text{‰}$ ), the results from samples 365.8, 547.4 and 828.6 agree remarkably well with their gas-source values (Fig. 6). In general, BSE homogeneity of a sample predicts low variance in distributions of  $\delta^{13}\text{C}$  values (although compositionally-similar phases from sample 712.8 show a large spread in  $\delta^{13}\text{C}$  values). The large variability in datasets from samples 44.4 and 712.8, by contrast, is well beyond measurement uncertainty. The dominant process controlling  $\delta^{13}\text{C}$  values in 712.8 likely is diagenesis. This sample is a dolomite-cemented sandstone, located at the top of a 50 m thick interval of siliciclastics (Fig. 1b). The positive mode in its  $\delta^{13}\text{C}$  distribution ( $\sim +4\text{‰}$ , Fig. 6) overlaps with the bulk carbon isotopic compositions of the directly overlying dolomitic stromatolite-microbialite unit ( $+1.7$  to  $+6.6\text{‰}$ ; Fig. 1b and c). This agreement suggests that at least some of the cement in sample 712.8 could have derived from fluids percolating downward, variably affecting the most permeable upper horizons, such as sandstones.

In sample 44.4, its complex  $\delta^{13}\text{C}$  distribution is related to its complex petrography. Imaging via BSE shows that the darker, Mn-poor calcite of this sample has ovate to spherical shapes, suggestive of the rounding expected for detrital grains of transported carbonate (Fig. 3e). The interpretation of detrital calcite also is supported by the morphology of grains in cathodoluminescence (CL) images (Fig. S17). These grains are ringed by halos of calcite that

are brighter under BSE, caused by Mn enrichment. This relationship suggests an alteration front, with recrystallization progressing inward from grain boundaries. The brighter calcite also appears to fill interstitial spaces between sedimentary grains (Fig. 3e), suggesting lithification by calcite cement richer in Mn. Importantly, however, these secondary alteration and cementation processes did not lower the  $\delta^{13}\text{C}$  value of the bulk rock (Fig. 6). The  $\delta^{13}\text{C}$  values of Mn-poor, detrital calcite overlaps isotopically with the population from Mn-rich calcite cements,  $-11.8 \pm 1.1\text{‰}$  vs.  $-10.7 \pm 1.1\text{‰}$  (Fig. 6f). A cross-plot between Mn and  $\delta^{13}\text{C}$  values shows a positive correlation (rank order correlation  $\rho = 0.66$ ,  $P = 0.05$ , Fig. S18), contrary to predictions that Mn-enrichment is associated with lower  $\delta^{13}\text{C}$  values in carbonates (Brand and Veizer, 1981).

The large variability in  $\delta^{13}\text{C}$  values from sample 44.4 is caused by measurements from dolomite – specifically, from dolomite cores ( $\delta^{13}\text{C}$  range of  $-5.0$  to  $+4.9\text{‰}$ ), as dolomite rims have values very similar to calcite ( $-10.0 \pm 1.1\text{‰}$ ). We interpret the presence of both euhedral (Fig. 4a–f) and anhedral (Fig. 4g–k) dolomite cores as a result of partial dissolution of some cores before formation of overgrowth rims. This process has been invoked to explain similarly irregularly-shaped dolomite cortices encased by euhedral dolomite rims in Tertiary dolomites from the Cayman Islands (e.g., Fig. 7 of Jones, 2005). In sample 44.4, dolomite rims all have planar, regular edges and rhombohedral shapes (Figs. 3c, d and 4), although partial dissolution features are present on some grain boundaries (e.g., Figs. 3c and 4a, b, and e). To account for such regular forms, we interpret these crystals (as large as  $35\text{ }\mu\text{m}$ ) to have grown unhindered in unoccluded sedimentary pore space before significant compaction or lithification had occurred.

### 4.2. Values of $\delta^{18}\text{O}$ and C–O covariation

Given the uniformity of  $\delta^{13}\text{C}$  values in samples 365.8 and 547.3 and the interpreted dominance of diagenetic processes in sample 712.8,  $\delta^{18}\text{O}$  values were measured for samples 44.4 and 828.6. These samples also span the GSMS  $\delta^{13}\text{C}$ – $\delta^{18}\text{O}$  range observed in this measured section (black symbols in Fig. 8). In sample 828.6, patterns in  $\delta^{18}\text{O}$  values are similar to those in  $\delta^{13}\text{C}$  (Figs. 6b and 7b). Distribution of values from both zoned and fine-



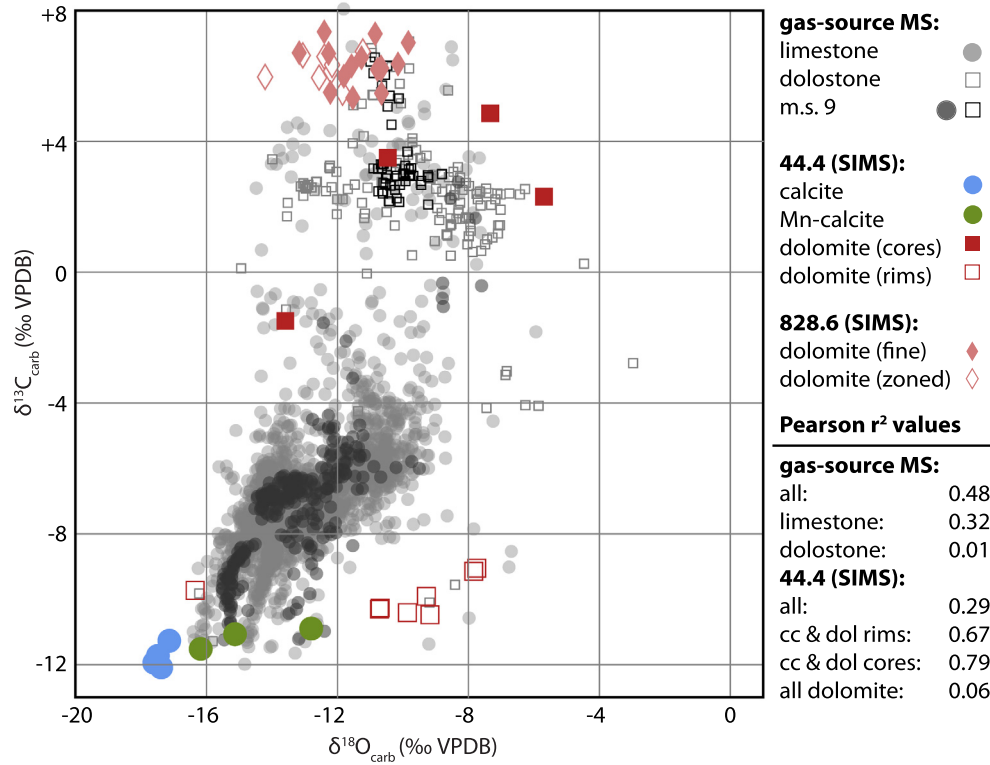


**Fig. 8.** Cross-plot of SIMS  $\delta^{13}\text{C}$  and  $\delta^{18}\text{O}$  values, coded by sample number (44.4 and 828.6) and carbonate phase. For reference, GSMS values from 12 measured sections of the Wonoka Formation (sections 1–12 of Husson et al., 2015b) are plotted also, coded as either limestone or dolostone. Measured section 9, from which the 5 SIMS samples were taken (Fig. 1b), is plotted as black, whereas the remaining GSMS data are gray.

grained dolomite overlap both with each other ( $-11.1 \pm 2.3\text{‰}$  and  $-12.3 \pm 2.0\text{‰}$ ) and with the GSMS value for this sample ( $-10.6\text{‰}$ ). Using the equation for dolomite-water fractionation from Horita (2014), these values ( $\delta^{18}\text{O} = -9$  to  $-14\text{‰}$ ) correspond to equilibration temperatures of  $70$ – $110^\circ$  with ice-free ocean waters ( $\delta^{18}\text{O} = -1\text{‰}$  VSMOW). These are reasonable burial temperatures for this sample, based on the minimum estimated thickness of sedimentary overburden at the section locality ( $2.0$ – $2.5$  km) and a typical geothermal gradient of  $25$ – $30^\circ/\text{km}$ . If the Ediacaran oceans were  $\sim 5\text{‰}$  more negative in  $\delta^{18}\text{O}$  value than the modern (Galili et al., 2019), the calculated temperature range shifts to  $45$ – $80^\circ\text{C}$ .

In sample 44.4, the distributions of  $\delta^{18}\text{O}$  values from dolomite rims and dolomite cores ( $-10.6 \pm 4.8\text{‰}$  and  $-9.4 \pm 5.5\text{‰}$ , respectively) overlap with values from 828.6 (Fig. 7a), although the distributions are more scattered. Calcite in this sample has tighter and more negative  $\delta^{18}\text{O}$  distributions (Fig. 7a), with Mn-poor calcite grains having the lowest  $\delta^{18}\text{O}$  value observed (down to  $-17.8\text{‰}$ ). Of the 71  $\delta^{18}\text{O}$  values acquired by SIMS, 42 can be paired with a  $\delta^{13}\text{C}$  value (Figs. S4–S10 and S15–S16). In a cross-plot (Fig. 8), SIMS results overlap with bulk GSMS values, and values from sample 44.4 show  $\delta^{13}\text{C}$  -  $\delta^{18}\text{O}$  covariation along two different arrays: between calcite and dolomite rims (Pearson  $r^2 = 0.67$ ), and another between calcite and dolomite cores ( $r^2 = 0.79$ ). Correlation is much weaker if all data from 44.4 is considered ( $r^2 = 0.29$ ), and disappears if calcite data are excluded ( $r^2 = 0.06$ ). A similar pattern is seen in the GSMS data from the Wonoka Formation (Fig. 8), where correlation is strongest when limestones and dolostones are considered together ( $r^2 = 0.48$ ), weaker if only limestones are included ( $r^2 = 0.32$ ) and non-existent when restricted to dolostones only ( $r^2 = 0.01$ ). At equilibrium, dolomite is predicted to be more positive in both  $\delta^{13}\text{C}$  and  $\delta^{18}\text{O}$  than calcite, although the difference is temperature-dependent (Figs. 8 and 9 in Horita, 2014) and cannot explain fully the observed correlations.

Although these data cannot offer a conclusive explanation for C-O covariation in ‘Shuram’ excursion carbonates, they do yield two important insights. First, the most negative  $\delta^{13}\text{C}$  (Fig. 6f) and  $\delta^{18}\text{O}$  values (Fig. 7a) were measured in sample 44.4 from the interior of rounded, detrital grains of calcite (Figs. 3e and S17). All secondary carbonate phases within this sample (Mn-rich calcite cement and dolomite) have more positive  $\delta^{18}\text{O}$  values. If dolomite  $\delta^{18}\text{O}$  values in sample 44.4 represent resetting at a range of burial depths and temperatures, then it is difficult to explain the observed calcite values of  $-17.8\text{‰}$  as a product of that same diagenetic history. Second, the small-scale gradients we see in  $\delta^{18}\text{O}$  values are impressive - in sample 44.4, the range is  $12\text{‰}$  across  $0.2\text{ mm}^2$  of analyzed surface (Fig. S1). Such variability is hard to reconcile with traditional models of carbonate diagenesis, wherein  $\delta^{18}\text{O}$  values becomes quickly fluid-buffered (e.g., Ahm et al., 2018). These SIMS data (Fig. 7a) imply that either sample 44.4 experienced very low water/rock ratios during its diagenetic history (at least after dolomite formation ceased), or that assumptions with regards to  $\delta^{18}\text{O}$  resetting need to be revisited.

#### 4.3. Implications for the Ediacaran carbon cycle

Given these observations, we propose the following depositional and diagenetic history for sample 44.4. Both detrital calcite and siliciclastic material were deposited in a turbidity current flowing downslope (Fig. 9a), consistent with petrographic observations (Fig. 3) and the interpreted depositional setting (Von der Borch et al., 1982; Husson et al., 2015b). The  $\delta^{13}\text{C}$  values of these rounded calcite grains were very negative ( $-11.8 \pm 1.1\text{‰}$ ). Once deposited, fluids infiltrated the sediment column before lithification (Fig. 9b), from which new carbonate was added as dolomite (Fig. 9c). The  $\delta^{13}\text{C}$  values of these phases require that dolomite growth was protracted - i.e., long enough to allow pore fluids to evolve from  $+5\text{‰}$  to  $-5\text{‰}$ , assuming this dolomite growth tracks

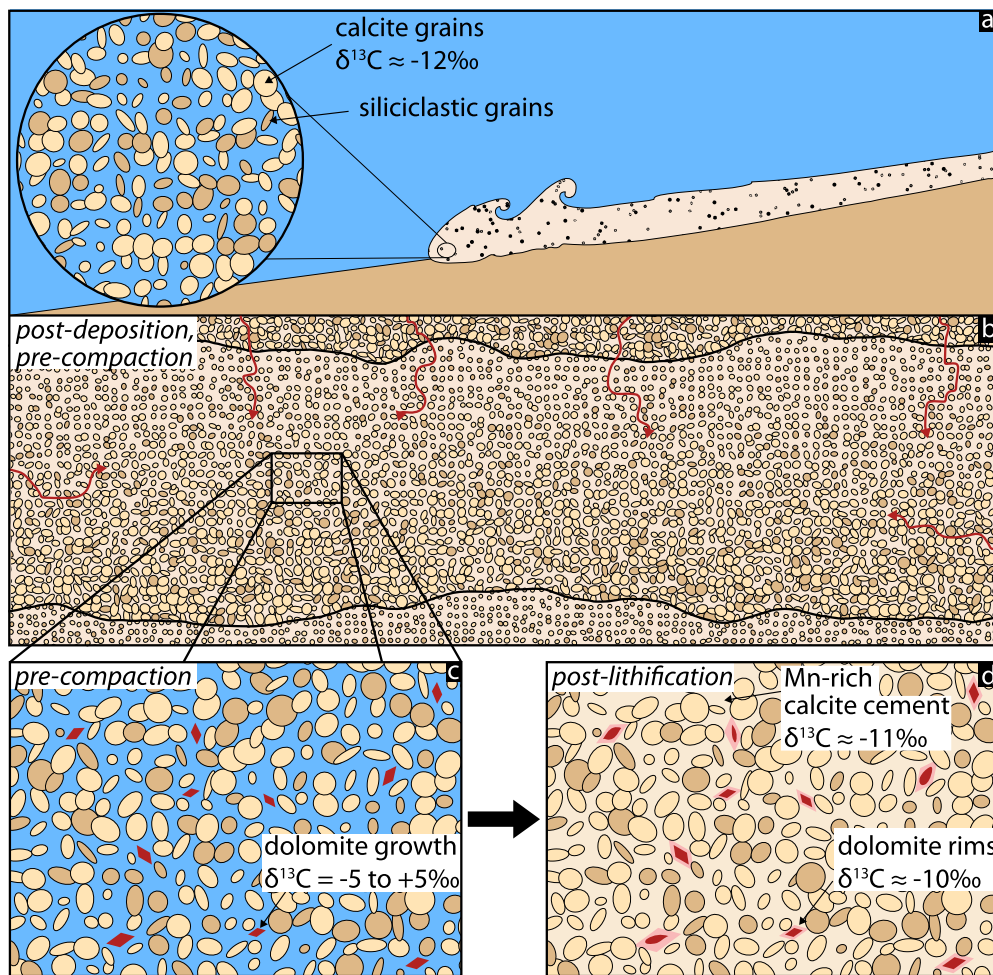


**Fig. 9.** Cartoon depicting the interpreted depositional and diagenetic events recorded in the basal Wonoka Formation. (A) Turbidity current carries both detrital siliciclastic and calcite material downslope, with calcite grains having  $\delta^{13}\text{C}$  values of  $\sim -12\text{‰}$ . (B) After deposition as a fining-upwards event bed, dolomite-forming fluids infiltrate the uncompacted strata. (C) New carbonate grows as dolomite in unoccluded pore space. (D) Initial dolomite growths are mantled by rims, and remaining porosity is filled with Mn-rich calcite.

the evolution of sedimentary pore fluids towards a rock-buffered state. This diagenetic dolomite was then mantled with a second generation of dolomite growth (Fig. 9d), distinct under BSE as overgrowths richer in Ca, Mn and Fe (darker cores and brighter rims in Figs. 3c and 4). When considering the  $\sim 2\text{‰}$  difference in fractionation factor between dolomite and calcite for temperatures  $< 100^\circ$  (Horita, 2014), the dolomite rims ( $-10.0 \pm 1.1\text{‰}$ ) have  $\delta^{13}\text{C}$  values equilibrated with the detrital calcite population and formed from a rock-buffered fluid. Likewise, the formation of Mn-rich calcite cement in the remaining interstitial spaces between grains was also rock buffered (Fig. 9d) and did not lower the  $\delta^{13}\text{C}$  value of the bulk rock (Figs. 6f and S18).

The observation that a detrital calcite phase carries the most negative  $\delta^{13}\text{C}$  values still allows the possibility of early diagenesis. Carbonate might have been altered isotopically up-slope, and then mobilized and redeposited as sedimentary beds. However, the bulk chemostratigraphic signal (Fig. 1c) is preserved with remarkable consistency across  $\sim 12,000 \text{ km}^2$  in South Australia (i.e., section-to-section differences in  $\delta^{13}\text{C}$  values are less than  $1\text{‰}$ , Husson et al., 2015b). This observation would demand identical degrees of carbonate diagenesis across the entire basin before transport. Thus, the most conservative explanation is that the low carbon isotope values originated in the water column in which these grains formed, before being transported downslope (Fig. 9a).

The dolomite cores of sample 44.4 (Fig. 4), however, complicate the meaning of these very low  $\delta^{13}\text{C}$  values. Interpreted to be au-

thigenic, these phases record a fluid(s) with an extremely different isotopic composition (up to  $+5\text{‰}$ , or greater) from the detrital calcite population. While dolostones exist in the uppermost Wonoka with  $\delta^{13}\text{C}$  values of  $+5\text{‰}$  (Fig. 1c), fluids from these horizons are not a likely source for the 44.4 dolomite cores. Even if pore-space could remain unoccluded in carbonate strata after  $\sim 800 \text{ m}$  (post-compacted) of burial (most pore space in Bahamian carbonate strata, by contrast, is closed after  $\sim 50 \text{ m}$  of burial, Melim et al., 2002), it is implausible for a fluid to remain  $+5\text{‰}$  after flowing downward through 100's of meters of carbonate strata with an average  $\delta^{13}\text{C}$  value of  $-8\text{‰}$  (Fig. 1c). The dolomites also are not likely to be organogenic (e.g., dolomite nodules of the Monterey Formation, Isaacs et al., 1987), as the Wonoka Formation is lean, with a total organic carbon average of 0.3% from unweathered drill core (Calver, 2000).

To explain these dolomites, the likeliest explanation is that distinct DIC pools, with both very positive and very negative  $\delta^{13}\text{C}$  values, were contemporaneous, with large lateral and/or vertical  $\delta^{13}\text{C}$  gradients in the surface environment. Detrital calcite grains formed in the negative pool before being transported downslope (Fig. 9a), and the dolomites sampled the positive pool during early marine diagenesis (Fig. 9b, c). These data are not the first to suggest large spatial heterogeneity in Ediacaran basin waters, and has been proposed previously to explain  $\delta^{13}\text{C}$  values in the Wonoka (Calver, 2000). In northwestern Canada, the nadir of stratigraphically-correlative negative  $\delta^{13}\text{C}$  excursions ranges from

−8.5‰ to −2‰ across the Mackenzie Mountains (Macdonald et al., 2013). In South China, the ‘Shuram’ excursion is not apparent in the most proximal sections of the Doushantuo Formation, and only reaches a minimum of ∼−6‰ in the most distal sections (Li et al., 2017). The challenges of correlating Precambrian strata, however, given the absence of biostratigraphy and the paucity of absolute age tie points, make the implications of these stratigraphic discrepancies ambiguous.

In the modern environment, the  $\delta^{13}\text{C}$  value of shallow-water DIC often diverges from the deep ocean average value. Near coastal waters can be affected by freshwater discharge from the continents carrying respired organic matter, as in the Florida Bay ( $\delta^{13}\text{C}$  of −7‰, Patterson and Walter, 1994). Carbon cycling in bank-top waters on the Bahamian carbonate platform leads to  $\delta^{13}\text{C}$  values of up to +2.3‰ (Geyman and Maloof, 2019; Swart et al., 2009), yielding carbonate mud of +5‰ owing to the equilibrium fractionation factor between aragonite and bicarbonate (Romanek et al., 1992). In pans of evaporating seawater in Israel, highly productive microbial mats can maintain DIC concentrations in disequilibrium with the atmosphere, leading to invasion of  $\text{CO}_2$  and a drop in  $\delta^{13}\text{C}$  value of DIC from +4 to −9‰ (Lazar and Erez, 1992). The mechanism proposed to explain this isotopic change in the brine was a kinetic isotope effect related to  $^{12}\text{CO}_2$  vs.  $^{13}\text{CO}_2$  hydration (McConnaughey, 1989). While 70% of initial seawater alkalinity precipitated as  $\text{CaCO}_3$ , the  $\delta^{13}\text{C}$  values of this carbonate were not measured (Lazar and Erez, 1992). This mechanism also is intriguing because it might result in carbonate with low  $\delta^{18}\text{O}$  values, thereby helping explain the correlation between  $\delta^{13}\text{C}$  and  $\delta^{18}\text{O}$  (Fig. 8). Whether disequilibrium processes, coupled with daily bursts of  $\text{CaCO}_3$  precipitation (Geyman and Maloof, 2019), could

lead to large volumes of isotopically negative carbonate sediment remains to be tested quantitatively.

We interpret the SIMS dataset of sample 44.4 as a result of large surface gradients in the  $\delta^{13}\text{C}$  values of DIC. The detrital calcite grain population sampled near-coastal waters that were affected by local processes (e.g., organic matter recycling,  $\text{CO}_2$  disequilibria). Early diagenetic dolomites sampled a DIC pool that remained positive in  $\delta^{13}\text{C}$ , which is consistent with the majority of Ediacaran carbonates (Halverson et al., 2005). The potential importance of local processes in governing carbon isotopic composition is consistent with  $\delta^{44/40}\text{Ca}$  values (Husson et al., 2015a). Large and stratigraphically coherent changes in  $\delta^{44/40}\text{Ca}$  are seen across the basin, with the highest values (−0.7‰, referenced to modern seawater) at the base, the lowest values (−1.8‰) in the middle part of the stratigraphy, and a return to high values again at the top of the Wonoka (−0.7‰, Husson et al., 2015a). Considering also strong correlations with Sr, Husson et al. (2015a) argued for carbonate mineralogical control on  $\delta^{44/40}\text{Ca}$  variability, as aragonite is depleted in  $^{44}\text{Ca}$  relative to calcite by ∼0.6–0.9‰ (Gussone et al., 2005), and dolomitization tends to increase  $\delta^{44/40}\text{Ca}$  values (Ahm et al., 2018). The  $\delta^{44/40}\text{Ca}$  value and Sr concentration of sample 44.4 are consistent with calcite as the original carbonate polymorph (Sr = 149 ppm,  $\delta^{44/40}\text{Ca}$  = −0.9‰); by contrast, original aragonite is indicated for samples 365.8 (Sr = 4400 ppm,  $\delta^{44/40}\text{Ca}$  = −1.9‰) and 547.3 (Sr = 2900 ppm,  $\delta^{44/40}\text{Ca}$  = −1.6‰). Owing to the metastability of aragonite (McIntyre, 1965), early neomorphism into calcite would have occluded available pore space in these samples, thus precluding the growth of early diagenetic dolomite, as seen in the (originally calcitic) sample 44.4.

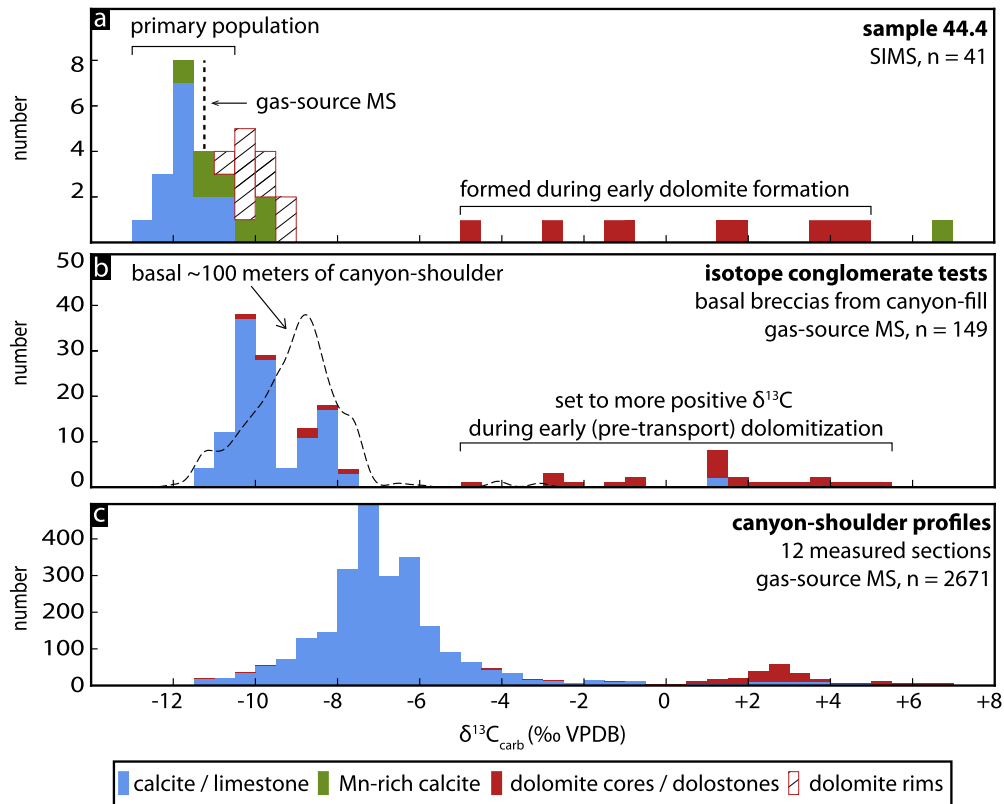


**Fig. 10.** A comparison of distributions of  $\delta^{13}\text{C}$  values from sample 44.4, Wonoka canyon-fill breccias and Wonoka canyon-shoulder profiles. (A) The SIMS results are binned and color-coded as in Fig. 6f and annotated according to the conceptual model presented in Fig. 9. (B) Values of  $\delta^{13}\text{C}$  values (GSMS) from three basal breccia units are binned and color-coded according to lithology (blue = limestone, red = dolostone). These units are the stratigraphically lowest breccia units from three different canyon-fill sequences (U1, U4 and O1 breccias of Husson et al., 2015b). (C) Values of  $\delta^{13}\text{C}$  values (GSMS) from 12 measured sections of the canyon-shoulder (sections 1–12 of Husson et al., 2015b) are binned and color-coded as in Fig. 10b. In panel B, dashed line is a scaled KDE of GSMS  $\delta^{13}\text{C}$  values of samples representing the lowermost ∼100 m of the canyon-shoulder sections (i.e., from below the erosional surface in Fig. 1b).



This pattern of calcium isotope variability means that  $\delta^{44/40}\text{Ca}$  and  $\delta^{13}\text{C}$  values strongly covary – negatively correlated for the lower half of the formation, and positively correlated for the upper half (Husson et al., 2015a). Strong correlations are not expected if both profiles record global seawater, given the order-of-magnitude difference between the residence times of carbon and calcium in the modern ocean ( $\sim 0.1$  Myr. and  $\sim 1$  Myr., respectively, Holmden et al., 2012). Why local carbonate mineralogy should also correlate with  $\delta^{13}\text{C}$ , however, remains unclear.

These SIMS results (Fig. 10a) also demand a refinement of the isotope conglomerate tests (see section 1, Fig. 10b). To explain the large range in  $\delta^{13}\text{C}$  values observed in basal breccia units of Wonoka canyon-fill ( $-11$  to  $+5.5\text{‰}$ , Fig. 10b), Husson et al. (2012) invoked the erosion and redeposition of carbonates from the Wonoka canyon-shoulder (range of  $-12$  to  $+8\text{‰}$ , Fig. 10c). In this interpretation, canyon-filling must have occurred after the majority of the canyon-shoulder had been deposited (Husson et al., 2012, 2015b). If basal canyon-fill sampled all horizons within the eroded interval with equal probability, the expectation is that the distribution of  $\delta^{13}\text{C}$  values in breccia clasts should be similar to the distribution of  $\delta^{13}\text{C}$  values from sampled canyon-shoulder sections (Fig. 10c). In the latter, values of  $\delta^{13}\text{C}$  from limestones appear normally distributed ( $-6.7 \pm 2.4\text{‰}$ ,  $1\sigma$ ) with a prominent mode at  $\sim -7\text{‰}$ , and dolostones are restricted generally to be greater than  $0\text{‰}$  (Fig. 10c). In the breccia clasts, by contrast, the distribution of limestones has a mean  $\delta^{13}\text{C}$  value of  $-9.7\text{‰}$  ( $\pm 0.9$ ) and no peak at  $-7\text{‰}$ . Dolostone clasts are distributed uniformly between  $-10.3$  and  $+5.5\text{‰}$  (Fig. 10b), and additionally have completely distinct  $\delta^{26}\text{Mg}$  values from canyon-shoulder dolostones (Fig. 9 from Husson et al., 2015a).

This pattern of carbon isotope variability – dolostones that are rare and widely dispersed in  $\delta^{13}\text{C}$  values, limestones with a comparatively tight  $\delta^{13}\text{C}$  distribution – is similar to the SIMS data from dolomite and calcite phases (Fig. 10a). Thus, it is most parsimonious to interpret the isotope conglomerate tests as a result of similar processes (e.g., Fig. 9). Eroded canyon-shoulder provided limestone clasts with very negative  $\delta^{13}\text{C}$  values (between  $-11$  and  $-8\text{‰}$ ). Canyon filling could have occurred after  $\sim 100$  m of canyon-shoulder deposition, coincident with a prominent erosional surface within the canyon-shoulder stratigraphy (Fig. 1b) that is responsible for some of the cut-fill sequences within the Wonoka (Haines, 1987; Husson et al., 2015b). Before being redeposited, some portion of this sampled canyon-shoulder population (dashed curve in Fig. 10b) was dolomitized by a fluid with positive  $\delta^{13}\text{C}$  values, resulting in dolostone clasts with carbon isotopic values of up to  $+5\text{‰}$  (Fig. 10b). This dolomitization process is observed in-situ with SIMS in sample 44.4 (Fig. 3). As with the SIMS results, this re-interpretation of the isotope conglomerate tests reinforces the need for very large  $\delta^{13}\text{C}$  gradients in the surface environment.

## 5. Conclusions

Coupled with a basin-wide view of the carbon isotope excursion (Husson et al., 2012, 2015b,a), these SIMS results reveal no significant role for post-depositional diagenesis in developing the observed negative excursion in  $\delta^{13}\text{C}$  in the Wonoka Formation. Local water DIC in this South Australian Ediacaran basin is the most probable origin for the signal. However, early diagenetic dolomites with  $\delta^{13}\text{C}$  values as high as  $+5\text{‰}$  co-occur with  $-12\text{‰}$  calcite detrital grains, which complicates interpretation of the excursion. We infer that isotopically-negative carbonate precipitation mainly occurred in shallow-water, platformal environments, with average deeper-water DIC not decreasing to  $-12\text{‰}$ . Assessing the possibility of large surface gradients in  $\delta^{13}\text{C}$  values of DIC is hampered by the dearth of independent correlation tie points within the Ediacaran Period, such as those provided by biostratigraphy or

geochronology. Thus, carbonate units correlative with 'Shuram' excursion sections would not be recognized as such if they do not have low  $\delta^{13}\text{C}$  values. It is notable, however, that at least 11 other Ediacaran basins distributed on 7 paleocontinents record carbon isotope excursions that are similar, pointing towards a global driver (Grotzinger et al., 2011). Developing a viable model that satisfies both the geological and geochemical observations remains an important and vexing problem for Neoproterozoic Earth history.

## Declaration of competing interest

The authors declare that they have no known competing financial interests or personal relationships that could have appeared to influence the work reported in this paper.

## Acknowledgements

Fieldwork and sample collection were supported by NSF grant EAR-1121034 to ACM and BS. Lab work was partially supported by NSF grant ICER-1440312 to SEP and the Department of Geoscience at the University of Wisconsin-Madison. WiscSIMS is supported by the NSF grants EAR-1355590 and EAR-1658823 and the University of Wisconsin-Madison. KK and AI were supported by the National Aeronautics and Space Administration under Grant NNA13AA94A issued through the Science Mission Directorate. JWV was supported by U.S. Department of Energy Office of Science, Office of Basic Energy Sciences, Chemical Sciences, Geosciences, and Biosciences Division under award number DE-FG02-93ER14389. We thank Brian Hess for sample preparation and John Fournelle and Bil Schneider for SEM imaging and EPMA. Mike Spicuzza calibrated calcite and dolomite standards by acid digestion and GSMS. We thank Clara Blättler and Anne-Sofie Ahm, who provided comments on a pre-draft of this manuscript. We thank 4 anonymous reviewers and Editor Lou Derry for their help and comments in making this work a better manuscript. We are grateful to the owners of Beltana Station for access to their land during fieldwork in South Australia.

## Appendix A. Supplementary material

Supplementary material related to this article can be found online at <https://doi.org/10.1016/j.epsl.2020.116211>.

## References

- Ahm, A.S.C., Bjerrum, C.J., Blättler, C.L., Swart, P.K., Higgins, J.A., 2018. Quantifying early marine diagenesis in shallow-water carbonate sediments. *Geochim. Cosmochim. Acta* 236, 140–159.
- Bergmann, K., 2013. Constraints on the carbon cycle and climate during the early evolution of animals (Chapter 2). PhD thesis. California Institute of Technology.
- Von der Borch, C., Smit, R., Grady, A., 1982. Late Proterozoic submarine canyons of Adelaide Geosyncline, South Australia. *Am. Assoc. Pet. Geol. Bull.* 66, 332–347.
- Brand, U., Veizer, J., 1981. Chemical diagenesis of a multicomponent carbonate system - 1: stable isotopes. *J. Sediment. Petrol.* 51, 987–997.
- Bristow, T., Kennedy, M., 2008. Carbon isotope excursions and the oxidant budget of the Ediacaran atmosphere and ocean. *Geology* 36, 863–866.
- Calver, C., 2000. Isotope stratigraphy of the Ediacaran (Neoproterozoic III) of the Adelaide Rift Complex, Australia, and the overprint of water column stratification. *Precambrian Res.* 100, 121–150.
- Cui, H., Kaufman, A.J., Xiao, S., Zhou, C., Liu, X.M., 2017. Was the Ediacaran Shuram excursion a globally synchronized early diagenetic event? Insights from methane-derived authigenic carbonates in the uppermost Doushantuo Formation, South China. *Chem. Geol.* 450, 59–80.
- Cui, H., Orland, I., Kitajima, K., Xiao, S., Kaufman, A., Fournelle, J., Baele, J., Goderis, S., Claeys, P., Valley, J., 2019. Probing an atypical Shuram excursion by SIMS. *Abstr. Program – Geol. Soc. Am.* 51.
- Derry, L.A., 2010. A burial diagenesis origin for the Ediacaran Shuram-Wonoka carbon isotope anomaly. *Earth Planet. Sci. Lett.* 294, 152–162.
- Farr, T.G., Rosen, P.A., Caro, E., Crippen, R., Duren, R., Hensley, S., Koblrick, M., Paller, M., Rodriguez, E., Roth, L., Seal, D., Shaffer, S., Shimada, J., Umland, J., Werner, M., Oskin, M., Burbank, D., Alsdorf, D., 2007. The shuttle radar topography mission. *Rev. Geophys.* 45, RG2004.

- Fike, D., Grotzinger, J., Pratt, L., Summons, R., 2006. Oxidation of the Ediacaran ocean. *Nature* 444, 744–747.
- Galili, N., Shemesh, A., Yam, R., Brailovsky, I., Sela-Adler, M., Schuster, E.M., Collom, C., Bekker, A., Planavsky, N., Macdonald, F.A., et al., 2019. The geologic history of seawater oxygen isotopes from marine iron oxides. *Science* 365, 469–473.
- Geyman, E.C., Maloof, A.C., 2019. A diurnal carbon engine explains  $^{13}\text{C}$ -enriched carbonates without increasing the global production of oxygen. *Proc. Natl. Acad. Sci.* 116, 24433–24439.
- Grotzinger, J., Fike, D., Fischer, W., 2011. Enigmatic origin of the largest-known carbon isotope excursion in Earth's history. *Nat. Geosci.* 4, 285–292.
- Gussone, N., Böhm, F., Eisenhauer, A., Dietzel, M., Heuser, A., Teichert, B., Reitner, J., Wörheide, G., Dullo, W., 2005. Calcium isotope fractionation in calcite and aragonite. *Geochim. Cosmochim. Acta* 69, 4485–4494.
- Haines, P., 1987. Carbonate shelf and basin sedimentation, late Proterozoic Wonoka Formation, South Australia. PhD thesis. University of Adelaide.
- Halverson, G., Hoffman, P., Maloof, A., Schrag, D., Rice, A.H.N., Bowring, S., Dudas, F., 2005. Toward a Neoproterozoic composite carbon-isotope record. *Geol. Soc. Am. Bull.* 117, 1181–1207.
- Holmden, C., Panchuk, K., Finney, S., 2012. Tightly coupled records of Ca and C isotope changes during the Hirnantian glaciation event in an epeiric sea setting. *Geochim. Cosmochim. Acta* 98, 94–106.
- Horita, J., 2014. Oxygen and carbon isotope fractionation in the system dolomite–water– $\text{CO}_2$  to elevated temperatures. *Geochim. Cosmochim. Acta* 129, 111–124.
- Husson, J.M., Higgins, J.A., Maloof, A.C., Schoene, B., 2015a. Ca and Mg isotope constraints on the origin of Earth's deepest  $\delta^{13}\text{C}$  excursion. *Geochim. Cosmochim. Acta* 160, 243–266.
- Husson, J.M., Maloof, A.C., Schoene, B., 2012. A syn-depositional age for Earth's deepest  $\delta^{13}\text{C}$  excursion required by isotope conglomerate tests. *Terra Nova* 24, 318–325.
- Husson, J.M., Maloof, A.C., Schoene, B., Chen, C.Y., Higgins, J.A., 2015b. Stratigraphic expression of Earth's deepest  $\delta^{13}\text{C}$  excursion in the Wonoka Formation of South Australia. *Am. J. Sci.* 315, 1–45.
- Isaacs, C.M., Petersen, N.F., Hein, J., 1987. Petroleum in the Miocene Monterey Formation, California. In: *Siliceous Sedimentary Rock-Hosted Ores and Petroleum: Evolution of Ore Fields*. Van Nostrand Reinhold, pp. 83–116.
- Jones, B., 2005. Dolomite crystal architecture: genetic implications for the origin of the Tertiary dolostones of the Cayman Islands. *J. Sediment. Res.* 75, 177–189.
- Kita, N.T., Ushikubo, T., Fu, B., Valley, J.W., 2009. High precision SIMS oxygen isotope analysis and the effect of sample topography. *Chem. Geol.* 264, 43–57.
- Knauth, L.P., Kennedy, M.J., 2009. The late Precambrian greening of the Earth. *Nature* 460, 728–732.
- Kozdon, R., Ushikubo, T., Kita, N., Spicuzza, M., Valley, J., 2009. Intratest oxygen isotope variability in the planktonic foraminifer *N. pachyderma*: real vs. apparent vital effects by ion microprobe. *Chem. Geol.* 258, 327–337.
- Lazar, B., Erez, J., 1992. Carbon geochemistry of marine-derived brines: I.  $^{13}\text{C}$  depletions due to intense photosynthesis. *Geochim. Cosmochim. Acta* 56, 335–345.
- Le Guerroué, E., Allen, P., Cozzi, A., 2006. Chemostratigraphic and sedimentological framework of the largest negative carbon isotopic excursion in Earth history: the Neoproterozoic Shuram Formation (Nafun Group, Oman). *Precambrian Res.* 146, 68–92.
- Li, C., Hardisty, D.S., Luo, G., Huang, J., Algeo, T.J., Cheng, M., Shi, W., An, Z., Tong, J., Xie, S., et al., 2017. Uncovering the spatial heterogeneity of Ediacaran carbon cycling. *Geobiology* 15, 211–224.
- Linzeimer, B.J., Kitajima, K., Denny, A.C., Cammack, J.N., 2018. Making maps on a micrometer scale. *Eos* 99.
- Lyons, T.W., Reinhard, C.T., Planavsky, N.J., 2014. The rise of oxygen in Earth's early ocean and atmosphere. *Nature* 506, 307–315.
- Macdonald, F.A., Strauss, J.V., Sperling, E.A., Halverson, G.P., Narbonne, G.M., Johnston, D.T., Kunzmann, M., Schrag, D.P., Higgins, J.A., 2013. The stratigraphic relationship between the Shuram carbon isotope excursion, the oxygenation of Neoproterozoic oceans, and the first appearance of the Ediacara biota and bilaterian trace fossils in northwestern Canada. *Chem. Geol.* 362, 250–272.
- McConnaughey, T., 1989.  $^{13}\text{C}$  and  $^{18}\text{O}$  isotopic disequilibrium in biological carbonates: I. Patterns. *Geochim. Cosmochim. Acta* 53, 151–162.
- McIntyre, W., 1965. The temperature variation of the solubility product of  $\text{CaCO}_3$  in sea water. Manuscript Report 200. Canada Fisheries Research Board, p. 153.
- Melini, L., Westphal, H., Swart, P., Eberli, G., Munnecke, A., 2002. Questioning carbonate diagenetic paradigms: evidence from the Neogene of the Bahamas. *Mar. Geol.* 185, 27–53.
- Patterson, W.P., Walter, L.M., 1994. Depletion of  $^{13}\text{C}$  in seawater  $\text{CO}_2$  on modern carbonate platforms: significance for the carbon isotopic record of carbonates. *Geology* 22, 885–888.
- Peters, S.E., Husson, J.M., Czaplewski, J., 2018. Macrostrat: a platform for geological data integration and deep-time earth crust research. *Geochim. Geophys. Geosyst.* 19, 1393–1409.
- Pu, J.P., Bowring, S.A., Ramezani, J., Myrow, P., Raub, T.D., Landing, E., Mills, A., Hodgins, E., Macdonald, F.A., 2016. Dodging snowballs: geochronology of the Gaskiers glaciation and the first appearance of the Ediacaran biota. *Geology* 44, 955–958.
- Raymond, O., Liu, S., Gallagher, R., Highet, L., Zhang, W., 2012. Surface Geology of Australia, 1:1 000 000 scale. 2012 edition [Digital Dataset]. Technical Report. Geoscience Australia. Commonwealth of Australia, Canberra.
- Romanek, C., Grossman, E., Morse, J., 1992. Carbon isotopic fractionation in synthetic aragonite and calcite: effects of temperature and precipitation rate. *Geochim. Cosmochim. Acta* 56, 419–430.
- Rothman, D., Hayes, J., Summons, R., 2003. Dynamics of the Neoproterozoic carbon cycle. *Proc. Natl. Acad. Sci.* 100, 8124–8129.
- Schrag, D.P., Higgins, J.A., Macdonald, F.A., Johnston, D.T., 2013. Authigenic carbonate and the history of the global carbon cycle. *Science* 339, 540–543.
- Śliwiński, M.G., Kitajima, K., Kozdon, R., Spicuzza, M.J., Denny, A., Valley, J.W., 2017. In situ  $\delta^{13}\text{C}$  and  $\delta^{18}\text{O}$  microanalysis by SIMS: a method for characterizing the carbonate components of natural and engineered  $\text{CO}_2$ -reservoirs. *Int. J. Greenh. Gas Control* 57, 116–133.
- Śliwiński, M.G., Kitajima, K., Kozdon, R., Spicuzza, M.J., Fournelle, J.H., Denny, A., Valley, J.W., 2016a. Secondary ion mass spectrometry bias on isotope ratios in Dolomite–Ankerite, part I:  $\delta^{18}\text{O}$  matrix effects. *Geostand. Geoanal. Res.* 40, 157–172.
- Śliwiński, M.G., Kitajima, K., Kozdon, R., Spicuzza, M.J., Fournelle, J.H., Denny, A., Valley, J.W., 2016b. Secondary ion mass spectrometry bias on isotope ratios in dolomite–ankerite, part II:  $\delta^{13}\text{C}$  matrix effects. *Geostand. Geoanal. Res.* 40, 173–184.
- Śliwiński, M.G., Kitajima, K., Spicuzza, M.J., Orland, I.J., Ishida, A., Fournelle, J.H., Valley, J.W., 2018. SIMS bias on isotope ratios in Ca–Mg–Fe carbonates (part III):  $\delta^{18}\text{O}$  and  $\delta^{13}\text{C}$  matrix effects along the magnesite–siderite solid-solution series. *Geostand. Geoanal. Res.* 42, 49–76.
- Swart, P.K., Reijmer, J.J., Otto, R., 2009. A reevaluation of facies on Great Bahama Bank II: variations in the  $\delta^{13}\text{C}$ ,  $\delta^{18}\text{O}$  and mineralogy of surface sediments. *Spec. Publ. Int. Assoc. Sedimentol.* 41, 47–59.
- Turnier, R.B., Katzir, Y., Kitajima, K., Orland, I.J., Spicuzza, M.J., Valley, J.W., 2020. Calibration of oxygen isotope fractionation and calcite–corundum thermometry in emery at Naxos, Greece. *J. Metamorph. Geol.* 38, 53–70.
- Valley, J.W., Kita, N.T., 2009. In situ oxygen isotope geochemistry by ion microprobe. In: *MAC Short Course*, vol. 41, pp. 19–63.